In Situ Studies of Precipitate Formation in Al-Pb Monotectic Solidification by X-Ray Transmission Microscopy

WILLIAM F. KAUKLER, FRANZ ROSENBERGER, and PETER A. CURRERI

Al-1.5 wt pct Pb monotectic alloys were unidirectionally solidified. X-ray transmission microscope (XTM) observations, both during and after solidification, revealed various new morphological/compositional features in the melt and solid. In the melt, nonuniform lead-rich interfacial segregation layers and droplets were observed to form well ahead of the interface. In the solid, periodic striae formed at translation/solidification velocities as low as 6×10^{-6} m/s. The striae shape does not replicate that of the interface. The striae spacing decreases from 4 to 2×10^{-4} m with an increasing solidification rate between 6 and 16×10^{-6} m/s. High resolution postsolidification XTM examination reveals that these striae consist of Pb-rich particles of 2 to 3×10^{-6} m diameter. At translation/solidification velocities below 6×10^{-6} m/s, Pb incorporation into the solid occurs in the form of continuous fibers and strings of particles of about 5×10^{-6} m diameter. Bands, parallel to the interface, in which these fibers were aligned in the solidification direction, alternated with bands of poor fiber alignment. The width of these bands is comparable to the striae spacings obtained at the high solidification rates.

I. INTRODUCTION

DUE to their inherent complexity, monotectic reactions have been investigated in less detail than the formation of eutectics or solid solutions. In particular, when the density of the second liquid, that forms on solidification, is higher than that of the original melt, sedimentation in the Earth's gravity field complicates detailed studies of such systems. Hence, there has been considerable interest in microgravity solidification of monotectic alloys.[1–17]

Metals are optically opaque. However, some insight into metallic solidification phenomena and their microstructural evolution has been obtained from transparent organic model systems.[14,18–20] But the details of the phase morphologies of the optically transparent systems and their thermophysical and transport properties differ significantly from metallic systems. Thus, there is a need for experimental techniques that allow real time determinations of the dynamics and morphology in metal systems.

X-ray transmission (or shadow) microscopy can image concentration gradients in the solid and liquid through differences in absorption. Traditional X-ray sources have been used to examine the homogeneity of thick specimens (of the order of millimeters),[21] to image shrinkage porosity during aluminum solidification,[22] melt-solid interface shape during Bridgman growth of germanium,[23] and convection caused by dissolving gold and silver wires in liquid sodium[24] with a resolution of 3 to 5×10^{-4} m. However, the imaging of microstructural features requires resolutions of 1 to 100×10^{-6} m.

Only recently have X-ray sources and detectors been advanced enough in resolution and contrast to allow system-atic studies of the relationship between melt dynamics and resulting microstructure. During our development of an X-ray transmission microscope (XTM) for solidification studies, we examined a number of alloys with which we had experience from prior microgravity research projects.[8,9] We have imaged the solidification of alloys in real time with resolutions of up to 3×10^{-5} m, employing a state-of-the-art 10 to 100 keV source, featuring a submicron focal spot.[1,2,3] Using solidifying aluminum alloys, we observed, in real time, the formation of the interfacial solute boundary layer in the liquid, interfacial morphologies, droplet coalescence, droplet incorporation, and particle/void engulfment by the advancing interface.

Our preliminary studies of monotectic alloy solidification with the XTM revealed various unexpected morphologies. Kaukler and Rosenberger[3] and Curreri and Kaukler[1,2] first demonstrated striation formation in such systems. In the present work, using recent improvements in the image resolution and contrast, we have further quantified striation formation in Al-Pb. The Al-1.5 wt pct Pb monotectic alloy is particularly well suited for X-ray solidification studies due to the good contrast provided by the large difference in X-ray absorptance between the immiscible phases. At lower solidification velocities, we found fine fibers and strings of Pb precipitates. Bands, parallel to the interface, in which these fibers were aligned in the solidification direction, alternated with bands of poor fiber alignment. In the following sections, after an outline of the experimental approach used, we will describe these observations in greater detail.

II. EXPERIMENT APPARATUS AND SAMPLE PREPARATION

The apparatus and details of exposure (X-ray energy and flux) employed for this study have been described in detail elsewhere.[1,2,3] Here, we will only outline the basic concept and essential features. In the projection radiography used, the specimen (in a furnace) is placed between the X-ray

WILLIAM F. KAUKLER, Assistant Research Professor, and FRANZ ROSENBERGER, Professor, are with the Center for Microgravity and Materials Research, University of Alabama in Huntsville, Huntsville, AL 35899. PETER A. CURRERI, Metals and Alloys Group Lead, Space Science Laboratory, NASA, Marshall Space Flight Center, AL 35812.
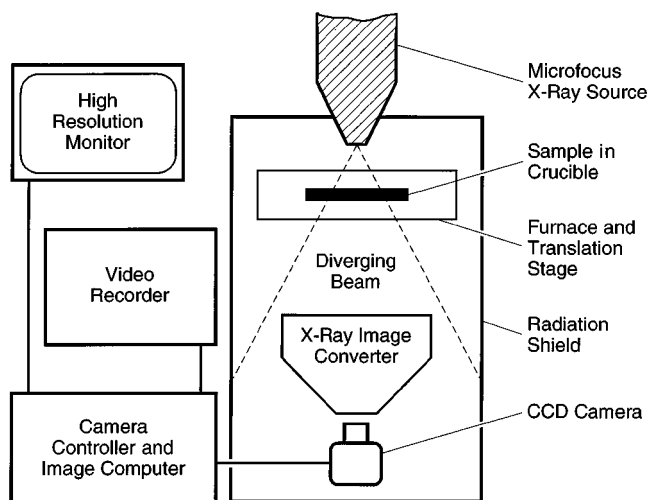
Fig. 1—X-ray transmission microscope: schematic diagram of components.
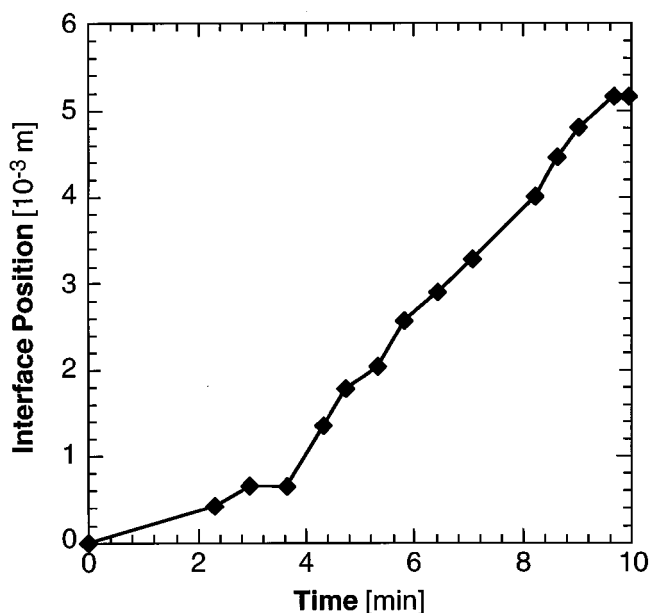

Fig. 2—Interface position *vs* time determined from *in situ* real-time radiomicrographs.

source and the X-ray image converter (Figure 1). In such an arrangement, the resolution and contrast are limited by the focal-spot size of the X-ray source, as well as the efficiency and spatial resolution of the image converter.[1,2] For maximum magnification, the distance between the source and sample should be minimized. Our current furnace design limits the magnification during solidification experiments to magnification 30 times. Solidified samples, removed from the furnace, can be brought close enough to the source to obtain magnifications of over 800 times.

With the current combination of X-ray image intensifier (Thompson CSF) and cooled CCD camera (Photometrics C200), differences in transmitted intensity as low as 2 pct can be detected. With the $<1 \times 10^{-6}$ m spot size used and the preceding magnification of 30 times, this allows for the resolution of 3×10^{-5} m diameter lead particles in 1-mm-thick Al samples during solidification. In postsolidification examination with magnification 500 times, lead

particles as small as 5×10^{-6} m can be resolved. This nonlinear interdependence of resolution and magnification is due to the feature-size-dependent degradation of the detector resolution.[1,2]

The furnace is designed for horizontal directional solidification. The sample is $5 \times 10^{-2} \times 2 \times 10^{-2}$ m and 1×10^{-3} m in transmission direction. It is completely enclosed in a flat boron nitride crucible to retain its shape during melting. The thin furnace housing is water cooled. Aluminum foil windows prevent excessive heat losses from the sample with a small attenuation of the X-ray flux. This design puts the specimen at least 1.1×10^{-2} m from the focal spot of the X-ray source. Using a single-zone heater arrangement, the temperature was stabilized to ± 0.1 K, and the temperature gradient in the vicinity of the interface was typically between 4.4 and 5.2×10^3 K/m. The interface was straight within 1×10^{-4} m across the sample; deviations from planarity in the vertical direction were even less.

A motor-driven screw pushes/pulls the specimen with its crucible at rates of 1 to 20×10^{-6} m/s normal to the X-ray beam. Due to the finite sample length, combined with actual interface displacements of up to 3.4×10^{-2} m, the heat transfer between the furnace and sample depends on the sample position. These end effects can cause the actual solidification velocities to exceed the translation rate from 30 to 45 pct. As a consequence, the interface location gradually drifts within the furnace window. For one sample, we determined the actual solidification rates and corresponding translation rates from video-recorded sequences of transmission images. The measured translation rate of 6.78×10^{-6} m/s was constant within better than 1 pct over 4×10^{-3} m. Figure 2 shows the measured interface position as a function of time. Note that by starting from a standstill, an initial transient is formed. From the fitted slope shown, an interface velocity of 11.4×10^{-6} m/s was obtained and found to be constant within 1.5 pct. In another set of experiments, an interface velocity of 12.8×10^{-6} m/s was obtained with a translation rate of 9.12×10^{-6} m/s.

Starting materials were 5/9 pure Al and Pb. Monotectic Al-1.5 wt pct Pb samples were prepared by melting in a graphite crucible, then rapidly solidifying in quartz tubes, followed by machining to the preceding dimensions. In spite of operation in air, oxidation of the molten samples was minimal in the tightly dimensioned BN crucibles.

Solidified, polished (but not etched) samples were analyzed for composition variation (a) with an electron microprobe by stepping along the specimen centerline in 1.5×10^{-5} m increments, counting for 3 seconds per step, and (b) by backscattered electron imaging in a scanning electron microscope (SEM).

III. RESULTS AND DISCUSSION

An XTM micrograph of solidifying Al-Pb is shown in Figure 3, with the melt on the left and solid on the right. As indicated, the translation rate was changed twice during solidification. Figure 3 clearly shows accumulation of the segregating Pb at the interface. However, this segregation, which is apparent at all translation rates above 6×10^{-6} m/s, is rather nonuniform along the interface. At 1.4×10^{-5} m/s, we estimate, from the local X-ray absorption, an increase in interfacial Pb concentration to at least 3 times the
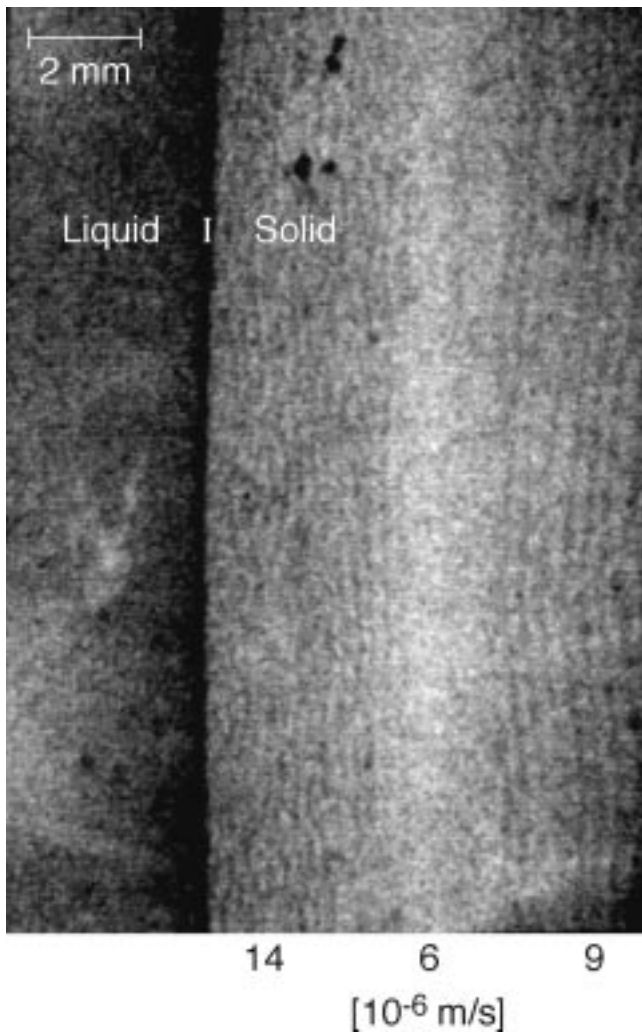
Fig. 3—X-ray radiomicrograph of Al-Pb monotectic during solidification showing solid-liquid interface (I). The solid formed at three different rates as indicated. Note the striae in the 9 and 14×10^{-6} m/s translation rate sections and the nonuniform Pb segregation along the interface in the melt.
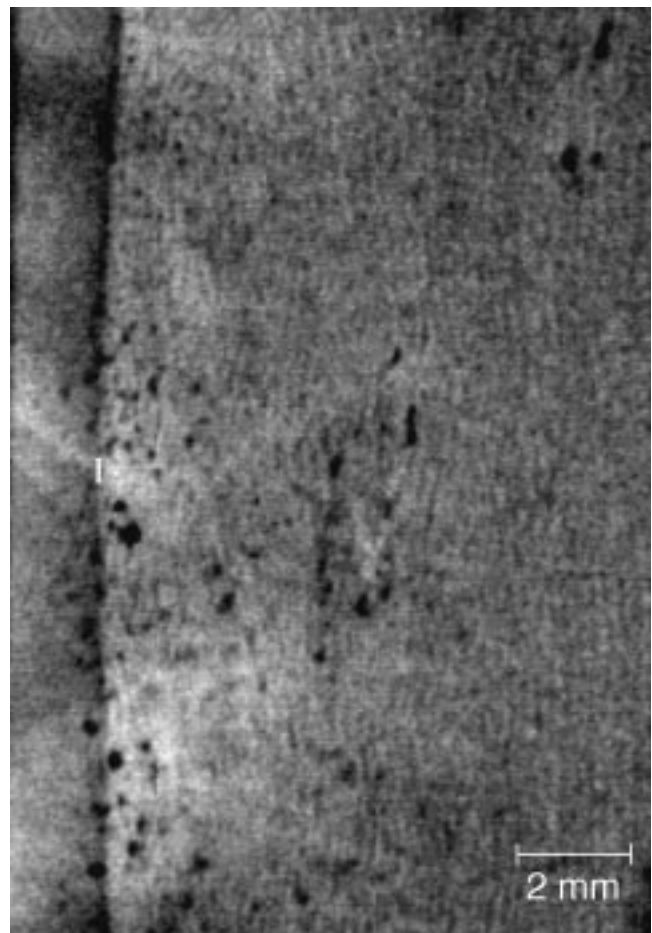

Fig. 4—Radiomicrograph obtained under same conditions as Fig. 3 at a later time. Note the coalescence of the rejected Pb into relatively large ($>35 \times 10^{-6}$ m diameter) droplets, which eventually become engulfed.
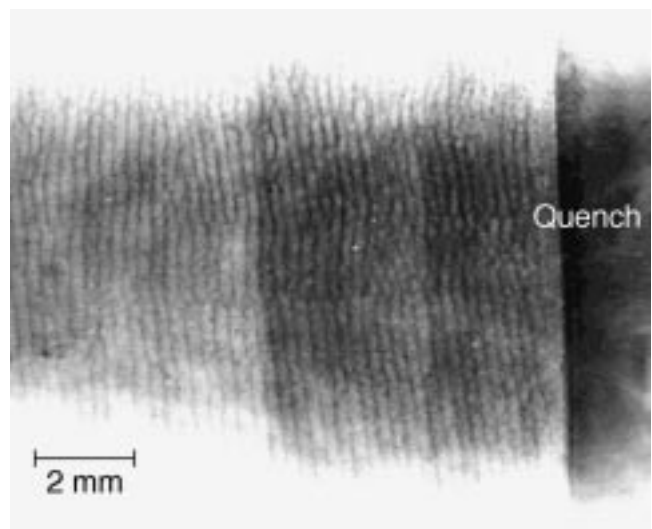

Fig. 5—Postsolidification low-magnification radiomicrograph. Growth direction from left to right; translation rate 9.1×10^{-6} m/s. Striations with $\approx 2.5 \times 10^{-4}$ m spacing and quenched interface at right.

bulk concentration. Interestingly, in spite of this high interfacial solute concentration, no morphological instabilities were observed. In contrast, with dilute Al-Cu and Al-Ag alloys, we found cellular or dendritic interfacial morphologies under similar solidification conditions at solidification rates above 2×10^{-6} m/s. On the other hand, at 1.4×10^{-5} m/s and above, it appears that relatively large drops of Pb-rich liquid (3 to 8×10^{-5} m diameter) form in the melt ahead of the interface. As indicated by Figure 4, the majority of these drops becomes incorporated into the solid which, in turn, results in a local decrease of the Pb concentration in the interfacial melt layer.

In the solid, Figure 3 reveals pronounced compositional striae with typical spacing of the order of 1×10^{-4} m. The maximum striae contrast is obtained at the sample location at which the X-ray propagation direction coincides with the striae ''plane,'' i.e., when a stria lies in the middle of the beam.[3] Note that the shape of the striae does not replicate that of the interface. The striae show local curvatures that largely exceed that of the interface at any time during the experiment. In addition, as can be seen particularly well in Figure 5, some of the striae actually intersect the interface.

From these observations, we can conclude that these striae are not simply the result of unsteadiness in the solidification rate that could result from unsteady sample temperature, translation rates, and convective transport.[25] One might
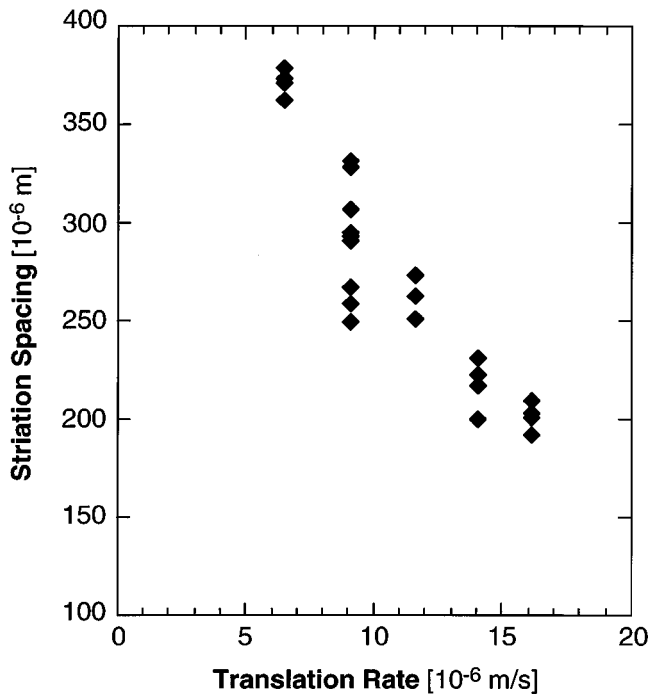
Fig. 6—Striation spacing *vs* translation rate obtained from all samples investigated. No striae were found below 6×10^{-6} m/s.
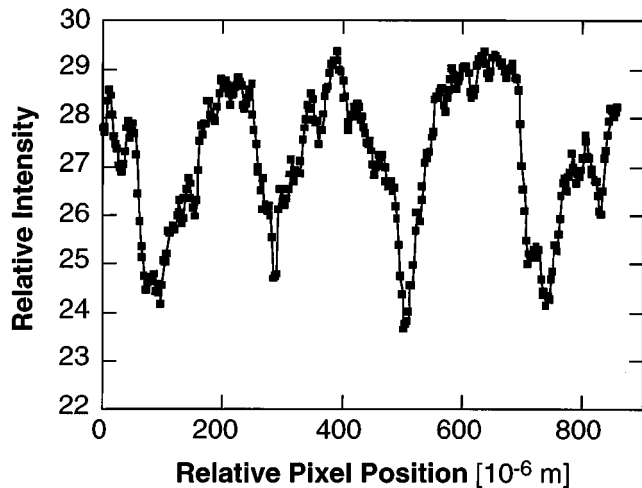

Fig. 7—Average pixel brightness *vs* position obtained from Fig. 5 in solidification direction (normal to the average striation length). Minima represent high Pb concentration.

Fig. 8—Electron microprobe profile of Pb counts across four striae of sample in Fig. 5. This profile was obtained from a 9.11×10^{-6} m/s segment of a unidirectionally grown specimen that was sectioned and mechanically polished.

speculate that the striae undulations seen in Figures 3 through 5 are somehow associated with the nonuniformity of Pb segregation along the interface, as previously discussed. At this point, however, our data are too sparse to support this mechanism over, say, a postsolidification precipitation scenario.

Note that the preceding striae formation has not been reported by others. Postsolidification examination of the previous samples by optical microscopy of metallographically prepared surfaces reveals only random spatial distributions of particles. As we will see later, these particles represent precipitates of the Pb-rich phase. Thus, the banding is only revealed by probing to a depth equal to or larger than the particle size. Similarly, faint indium-rich striae in Al-In monotectics were only revealed by high magnifica-
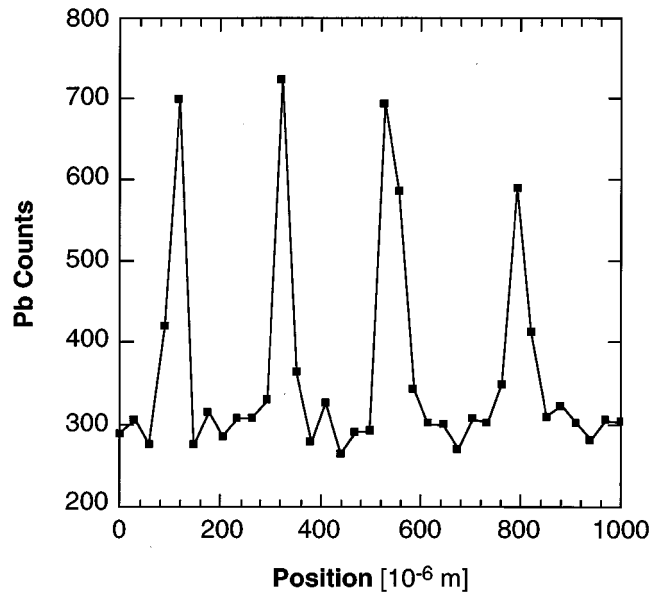
tion XTM postsolidification analysis.[1,2] From this, we propose that such striae (in monotectic alloys) may be a rather widespread phenomenon.

The dependence of striae spacing on translation rate was studied by *in situ* observation of six Al-Pb monotectic specimens solidifying at various rates. Figure 5 shows a postsolidification transmission radiograph of a section of one sample solidified at 9.1×10^{-6} m/s. The dark zone on the right is the result of sample quenching. Striation spacings were determined by averaging over 10 to 20 striae at various locations across the width of the specimen. In Figure 6, the measured spacings are plotted *vs* translation rate. The scatter in the data at a given translation rate is due to the thermal end effects in different samples, as discussed previously. One sees that the average spacings decrease roughly linearly from 4 to 2×10^{-4} m on increasing the translation rate from 6 to 17×10^{-6} m/s. Note that below about 6 to 7×10^{-6} m/s, no striae are observed.

The solute bulk distribution across striae was determined through optical density profiles of radiomicrographs parallel to the translation direction. Scan widths of 70 pixels resulted in relatively smooth contours. Narrower width scans produced considerably greater scatter. Such a scan corresponding to 1 mm on the sample of Figure 5 is reproduced in Figure 7. The peaks in the profile (maxima in X-ray transmission) represent regions of minimum Pb content. This image shows that the Pb-rich bands constitute about 25 pct of the striae spacing.

To determine the sample thickness required to discern the striae, which, as mentioned previously, were not revealed by optical surface inspection, we have investigated the composition of the top 2 to 3×10^{-6} m by high energy (30 to 35 kV) electron microprobe and backscattered electron imaging. Figure 8 shows the Pb signature obtained in a 1×10^{-3} m long electron microprobe scan (30 keV, scanning width 3×10^{-5} m, and 1.5×10^{-5} m steps) across four striae of the sample of Figure 5. No lead was detected
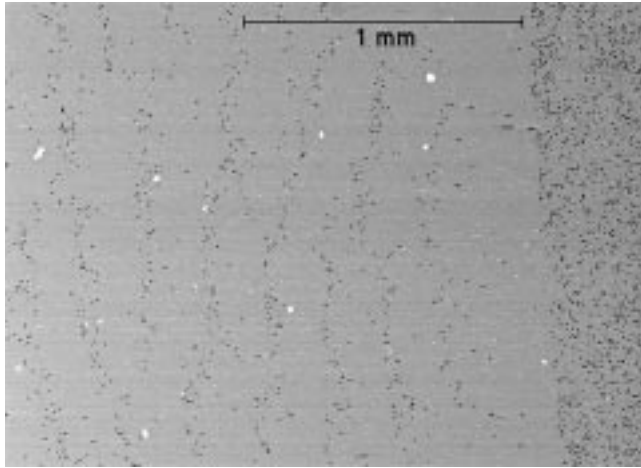
Fig. 9—Backscattered electron image of polished (unetched) longitudinal section of Al-Pb monotectic unidirectionally solidified from left to right at 9.11×10^{-6} m/s in 4.7×10^3 K/m gradient. Dark spots represent Pb-rich particles. Right edge of image shows quenched interface.
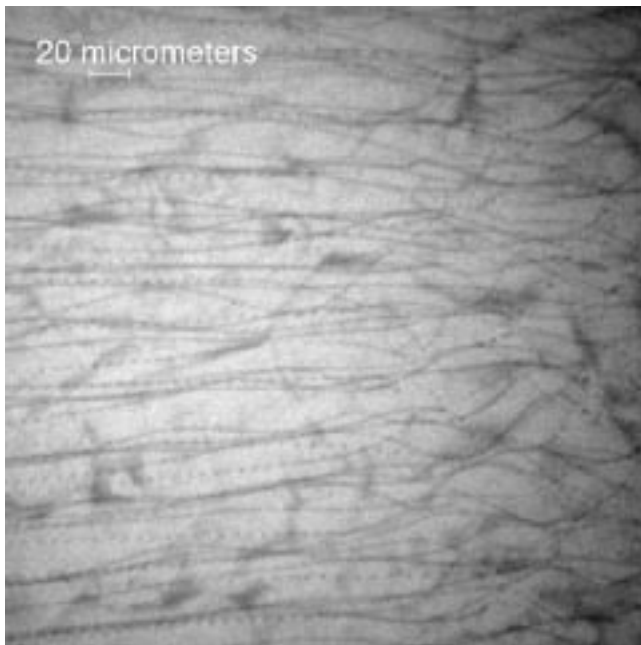

Fig. 10—High-magnification postsolidification radiograph of sample solidified at 2.9×10^{-6} m/s. Growth direction from right to left. Note the well-aligned Pb fibers and strings (left side) and their poor alignment on the right.
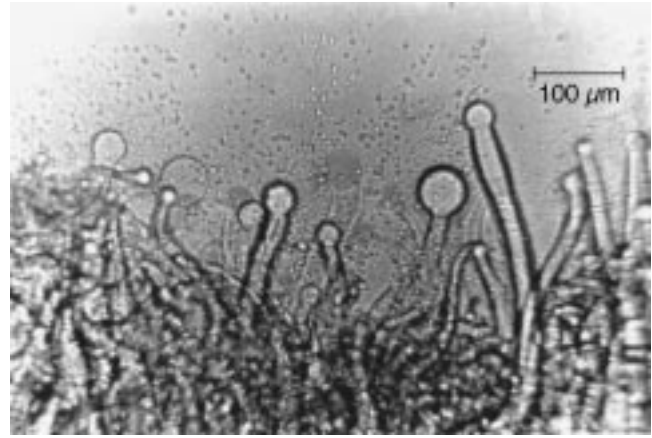

Fig. 11—*In situ* optical micrograph of succinonitrile-benzene monotectic, 34 mol pct benzene, solidifying in upward direction at 2×10^{-6} m/s in a 1.5×10^{-4} m thick cell with a temperature gradient of about 6×10^3 K/m. Droplets of L_2 are forming at the tips of the tubular stalks, which are the result of the solidification reaction. The melt, at the top, is the L_1 phase from which these two monotectic phases form. Note the worm morphology of the stalks.

between the striae. The 2.5×10^{-4} m peak-to-peak spacing of the Pb counts agrees well with the striation spacing obtained for this solidification rate from the radiographs. Note that standard examination with low-energy SEM, due to the low penetration depth, would not have revealed these features.

The backscattered electron image presented in Figure 9 shows that the striae consist of randomly positioned Pb particles. Again, striation spacings obtained with this technique agree well with values determined from low magnification radiographs. Particle diameters deduced from magnification 1000 times backscattered electron images show a rather monodisperse distribution of spherical particles centering around 2.5 to 3×10^{-6} m. At this point, it is not clear whether these particles represent solidified Pb droplets that were engulfed by the advancing interface or formed after solidification through diffusion/precipitation. The region at the right edge of Figure 9 is the quenched liquid zone, which corresponds to the quenched region in Figure 5. Its higher particle concentration is consistent with the strong rejection of solute at the solid-melt interface. Most particles in the quench zone, with the exception of a few larger ones, are of the same size as those in the striae. This fact supports the precipitation mechanism for particle formation.

As mentioned previously, no striae were obtained at translation rates below 6 to 7×10^{-6} m/s. However, magnification 400 times postsolidification XTM radiography of a specimen solidified at 2.9×10^{-6} m/s resolved delicate fibers and strings of particles (''necklaces'') with rather uniform diameters of about 5×10^{-6} m (Figure 10). Interestingly, without apparent changes in the solidification parameters, there is a succession of bands in which the fibers/necklaces are relatively well aligned (left region in Figure 10) and bands in which they rather randomly meander in three dimensions (right region in Figure 10). The distance between regions of fiber misalignment was comparable to the striae spacing of 2×10^{-4} m. Stereo XTM imaging shows that the fibers/necklaces remain approximately equidistant inspite of the three-dimensional meandering.

It should be emphasized that during the preceding real-time XTM observations, the interfaces remained planar within the resolution limit of several 10^{-5} m. One could be tempted to view the necklace morphologies as a sign of a ripening mechanism and solid-state diffusion.[26,27] But the fact that neighboring fibers remain intact does not support this. Obviously, more work is required to resolve this issue.

It should be pointed out that the meandering fiber morphology observed in the Al-Pb system closely resembles the ''worms'' obtained in six succinonitrile-based monotectics;[14,20] *e.g.*, the morphology obtained in succinonitrile-benzene depicted in Figure 11. These worms initially form as tubes of succinonitrile (the solid phase forming in this system) filled with benzene (L_2) through continuous solid-

ification from larger benzene droplets (Figure 11). As the interface advances, the spaces between the solid tubes become filled with the remainder of the solidifying matrix. The close resemblance of morphologies obtained in these organic monotectics and the findings for the Al-Pb system presented here suggest a similar mechanism for the phase separation. However, unambiguous evidence for this analogy through direct observation of worm formation in opaque metallic monotectic alloys must await further improvements in the resolution of the XTM system.

IV. SUMMARY AND CONCLUSIONS

Real-time and postsolidification X-ray transmission microscopy reveals various three-dimensional compositional inhomogeneities in Al-Pb monotectics that cannot be detected by traditional metallurgical inspection.

We found that the nucleation of the second liquid phase does not necessarily occur at the solid-liquid interface. Lead-rich droplets of up to 8×10^{-5} m were observed to form several 1×10^4 m ahead of the solid phase at translation/solidification rates in excess of about 1×10^{-5} m/s. The droplets were engulfed by the solid.

Segregation features in the solid included bands and strings of Pb-rich particles, as well as continuous Pb-rich fibers. The bands or striae, which formed at translation/solidification rates exceeding 6×10^{-6} m/s, typically did not replicate the shape of the respective interface and consisted of monodisperse particles 2.5 to 3×10^{-6} m in diameter. Fibers and strings, which formed at lower solidification rates, were, on average, oriented normal to the interface, which remained planar during solidification. However, the morphology of both features alternates from good alignment in the solidification direction to strong local curvature in periodic bands parallel to the interface. The width of these bands is comparable to the striae spacings obtained at the high solidification rates. Fibers and strings appeared in close proximity and possessed the same diameter of about 5×10^{-6} m. This renders a simple post-solidification ripening mechanism for the formation of strings from fibers unlikely. Furthermore, bands, parallel to the interface, in which the fibers were aligned in the solidification direction, alternated with bands of poor fiber alignment.

ACKNOWLEDGMENTS

REFERENCES

1. P.A. Curreri and W.F. Kaukler: *7th Int. Symp. on Experimental Methods for Microgravity Materials Science*, TMS, Warrendale, PA, 1995, pp. 93-101.
2. P.A. Curreri and W.F. Kaukler: *Metall. Mater. Trans. A*, 1996, vol. 27A, pp. 801-08.
3. W.F. Kaukler and F. Rosenberger: *Metall. Mater. Trans. A*, 1994, vol. 25A, pp. 1775-77.
4. G.H. Otto: *Proc. 5th Eur. Symp. on Material Science under Microgravity*, Schloss-Elmau, Nov. 5–7, 1984, ESA SP-222, European Space Agency, Paris, France, Dec., 1984, pp. 379-88.
5. D. Langbein: *Proc. Norderney Symp. on Scientific Results of the German Spacelab Mission D1*. BMFT, Federal Republic of Germany, Norderney, Germany, Aug. 27–29, 1986, pp. 101-02.
6. L.L. Lacy and C.Y. Ang: *Apollo Soyuz Test Project Summary Science Report, Vol. 1* NASA SP-412, NASA, Washington, DC, 1977, pp. 403-28.
7. J.L. Reger: *Proc. 3rd Space Processing Symp. Skylab Results, Vol. I*, Apr. 30–May 1, 1974, NASA, Marshall Space Flight Center, AL, pp. 133-58.
8. P.A. Curreri and W.F. Kaukler: NASA Technical Memorandum, NASA-TM-86573, NASA, Marshall Space Flight Center, AL, Nov. 1986.
9. M.K. Wu, J.R. Ashburn, P.A. Curreri, and W.F. Kaukler: *Metall. Trans. A*, 1987, vol. 18A, pp. 1511-17.
10. B.K. Dhindaw, D.M. Stefanescu, A.K. Singh, and P.A. Curreri: *Metall. Trans. A*, 1988, vol. 19A, pp. 2839-46.
11. J.B. Andrews, A.C. Sandlin, and P.A. Curreri: *Metall. Trans. A*, 1988, vol. 19A, pp. 2645-50.
12. A.C. Sandlin, J.B. Andrews, and P.A. Curreri: *Metall. Trans. A*, 1988, vol. 19A, pp. 2665-69.
13. *Materials Science on Parabolic Aircraft*, NASA TM-4456, P.A. Curreri, ed., NASA, Marshall Space Flight Center, AL, Mar. 1993.
14. W.F. Kaukler and D.O. Frazier: *J. Cryst. Growth*, 1985, vol. 71, pp. 340-45.
15. P.D. Caton and W.G. Hopkins: *Proc. 3rd Eur. Symp. on Material Science in Space*, Grenoble, Apr. 24–27, 1979, ESA SP-142, European Space Agency, Paris, France, June 1979, pp. 89-94.
16. W.G. Hopkins: *The Effect of Gravity on Immiscible Alloys*, ESA SP-219, European Space Agency, Paris, France, Mar. 1984, pp. 83-86.
17. J. Cremin: *AIAA Space Programs and Technologies Conf.*, Sept. 25–28, 1990, Huntsville, AL, AIAA paper no. 90-3539.
18. K.A. Jackson and J.D. Hunt: *Acta Metall.*, 1965, vol. 13, p. 1212.
19. R. Trivedi, J.A. Sekhar, and V. Seetharaman: *Metall. Trans. A*, 1989, vol. 20A, pp. 769-77.
20. W.F. Kaukler and D.O. Frazier: *Nature*, 1986, vol. 323 (6083), pp. 50-52.
21. B. Lindstrom: in *X-ray Optics and X-ray Microanalysis*, H.H. Pattee, V. Cosslett, and A. Engstrom, eds., Academic Press, New York, NY, 1963, pp. 13-22.
22. F.P. Chiaramonte, G.F. Danier, J. Gotti, E.S. Neumann, J. Johnston, and K.J. De Witt: *AIAA 30th Aerospace Sciences Meeting*, Reno, NV, Jan. 6–9, 1992, AIAA paper no. 92-0845.
23. P.G. Barber, R.F. Berry, W.J. Debnam, A.L. Fripp, G. Woodell, and R.T. Simchick: *J. Cryst. Growth*, 1995, vol. 147, pp. 83-90.
24. G.R. Chappleman: *J. Mater. Sci.*, 1982, vol. 17, p. 2208.
25. F. Rosenberger: *Fundamentals of Crystal Growth*, Springer, New York, NY, 1979, Sec. 6.5.1.
26. H. Song and A. Hellawell: *Metall. Trans. A*, 1989, vol. 20A, pp. 171-77.
27. S.C. Sarson and J.A. Charles: *Mat. Sci. Technol.*, 1993, vol. 9, pp. 1049-61.